

# Scattering of energetic electrons through nonlinear cyclotron resonance with coherent whistler-mode hiss emissions

Cite as: Phys. Plasmas **29**, 112901 (2022); doi: [10.1063/5.0106004](https://doi.org/10.1063/5.0106004)

Submitted: 27 June 2022 · Accepted: 1 October 2022 ·

Published Online: 4 November 2022



View Online



Export Citation



CrossMark

Miwa Tobita<sup>1,a)</sup>  and Yoshiharu Omura<sup>2,b)</sup> 

## AFFILIATIONS

<sup>1</sup>Graduate School of Engineering, Kyoto University, Kyoto 615-8510, Japan

<sup>2</sup>Research Institute for Sustainable Humanosphere, Kyoto University, Kyoto 611-0011, Japan

<sup>a)</sup> Author to whom correspondence should be addressed: [tobita.miwa.73x@st.kyoto-u.ac.jp](mailto:tobita.miwa.73x@st.kyoto-u.ac.jp)

<sup>b)</sup> Electronic address: [omura@rish.kyoto-u.ac.jp](mailto:omura@rish.kyoto-u.ac.jp)

## ABSTRACT

Recent observations have revealed that plasmaspheric hiss consists of many discrete waves called “hiss elements.” However, the interaction of energetic electrons (10 keV to several MeV) with the plasmaspheric hiss has only been simulated by the quasilinear (QL) diffusion theory, which does not take the fine wave structure into account. The QL theory cannot address nonlinear particle motions determined by the inhomogeneity factor, which influences the scattering of electrons in pitch angle and energy. This study aims to identify differences between the nonlinear wave–particle interaction and QL theory for plasmaspheric hiss emissions. We conduct test particle simulations to demonstrate the nonlinear interactions between hiss waves and electrons. The nonlinear theory is used to model hiss elements consisting of discrete frequencies and continuous phases. Unlike the other theories, the frequency and amplitude variations in time of the hiss packet are taken into account. Frequencies of the packets are determined to satisfy the separability criterion; when the criterion is met, resonance overlapping is absent, and the electrons can generate each wave element independently. The realistic simulation model of hiss waves reproduces the scattering of electrons by both first- and second-order resonances. We also evaluate the efficiency of electron scattering by calculating nonlinear diffusion coefficients. The diffusion coefficient of equatorial pitch angle is of the same order of magnitude as those calculated by the QL diffusion theory, while we find the effective acceleration of resonant electrons by successive nonlinear trapping, which is not evaluated by the QL theory.

Published under an exclusive license by AIP Publishing. <https://doi.org/10.1063/5.0106004>

## I. INTRODUCTION

Whistler-mode waves play essential roles in the acceleration and precipitations of energetic electrons in the earth’s magnetosphere. Whistler-mode waves naturally occurring in the equatorial magnetosphere fall into two categories with specific features in dynamic frequency spectra: one is called chorus, and the other is called hiss. Chorus consists of strong discrete elements with rising-tone or falling-tone frequencies over a range  $0.1\text{--}0.7 f_{ce}$ , where  $f_{ce}$  is the electron cyclotron frequency. Each chorus element lasts hundreds of milliseconds and is observed outside the plasmasphere. On the other hand, hiss consists of many wave elements with small frequency variation scattered over a wide frequency range below about  $0.1 f_{ce}$ . Each hiss element lasts over a few tens of milliseconds and is observed nearly continuously inside the plasmasphere.

The quasilinear (QL) diffusion theory for whistler-mode waves has been developed to derive rates of pitch angle and energy scattering

by electromagnetic waves, including plasmaspheric hiss.<sup>1,2</sup> The theory assumes the first-order resonance and analyzes weak plasma turbulence by expanding the collisionless Boltzmann equation. The gyro-phases of the particles are averaged to embed the cyclotron resonance in the diffusion equation, but the second-order resonance, such as phase trapping and bunching of electrons during the cyclotron resonance,<sup>3,4</sup> is not taken into account. During the second-order resonance, the difference between the wave phase and the electron’s gyrophase remains constant for a certain period. Summers *et al.*<sup>2</sup> obtained a diffusion coefficient for pitch angle scattering, and the corresponding timescale for atmospheric precipitation is 1 h to several days for 100 keV to several MeV electrons in the outer radiation belt. It also reported that the diffusion coefficient for energy scattering by hiss is a few thousand times smaller than the one by chorus emissions, which indicates that hiss emissions do not efficiently contribute to the acceleration of electrons. Through test particle simulations based on

self-consistent wave fields in a particle code, Allanson *et al.*<sup>5</sup> studied the validity of the QL diffusion theory with different amplitudes of incoherent whistler-mode waves and found that the advective component of electron dynamics appears for large-amplitude waves as well as diffusive component.

In recent years, however, high-resolution data observed by Van Allen probes revealed that plasmaspheric hiss has a fine wave structure with discrete frequencies propagating from the equator.<sup>6–8</sup> We call each wave structure “hiss packets,” whose amplitude distributions are limited in time and space. The analysis in Ref. 6 has confirmed that the phase of each packet is continuous in time. This structure can cause successive nonlinear interactions. Electrons are expected to be in both first- and second-order resonance with the packets one after another. Some of them can experience phase trapping, causing effective scattering of electrons in pitch angle and energy.

Different models have been proposed as the origin of plasmaspheric hiss. In the present study, partly because of the observations of plasmaspheric hiss introduced earlier and partly because of recent simulation studies showing the generation of hiss emissions through nonlinear interaction with energetic electrons,<sup>9–11</sup> we assume that hiss emissions are generated locally in the equatorial region inside the plasmasphere through coherent nonlinear wave–particle interaction with energetic electrons injected into the plasmasphere.<sup>7</sup>

In this paper, test particle simulations are conducted with the existence of the fine structure of coherent hiss packets. Waves with continuous phases are constructed based on a nonlinear theory developed for hiss in Ref. 7. The time evolution of the wave frequency and amplitude is also included in the simulation based on the nonlinear theory. The motion of electrons is calculated with the presence of the waves. Several recent studies<sup>12–14</sup> conducted test particle simulations targeting the chorus waves to explore the boundary between nonlinear and QL framework; the present study is the first trial of test particle simulations based on the nonlinear theory focusing on the plasmaspheric hiss.

## II. SIMULATION SETTING

We assume a one-dimensional system along  $z$ -axis to simulate energetic electrons interacting with a plasmaspheric hiss. The relation of the  $z$ -axis to the real system is shown in Fig. 1. The positive direction of  $z$ -axis is taken parallel to the background magnetic field  $B_0$ . The point  $z = 0$  corresponds to the equator. The length of the system is limited to the range  $|z_{\max}| < 500c/\Omega_{e0}$ . The equations of wave propagation and the motion of electrons are solved in the spatially limited system. We assume that waves do not exist outside the system. The waves are deleted when they reach the end of the system in the simulation, and the particles undergo adiabatic motion outside the system. The parallel velocities of electrons are changed in sign when they reach the system’s end. The lapse time for particles to undergo adiabatic motion outside the system is not considered.

The background magnetic field is defined by a cylindrical model

$$B_0(z) = B_{e0}(1 + az^2). \quad (1)$$

The parabolic coefficient  $a$  is calculated by  $a = 4.5/(L^2 R_E^2)$ , where  $L$  is the distance along the magnetic field line from the center of the earth at the equator normalized by the radius of the earth  $R_E$ . According to Eq. (1), the local cyclotron frequency of an electron  $\Omega_e$  is given by

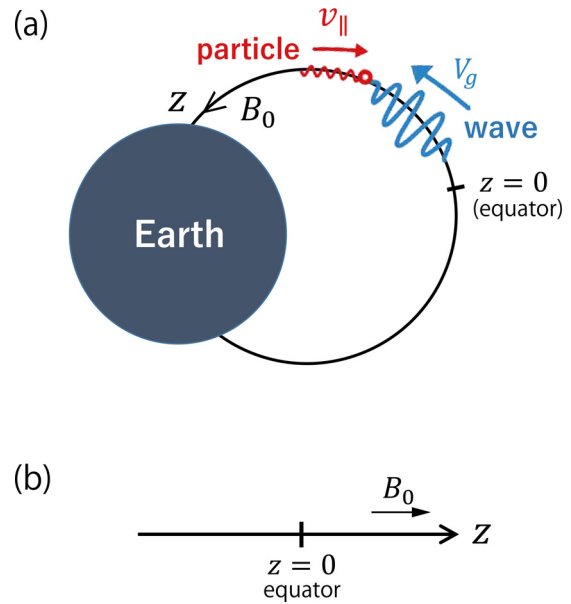


**FIG. 1.** (a) Schematic illustration of the interaction between waves and electrons. The coordinate  $z$  is introduced as an axis along the earth’s magnetic field  $B_0$ . The origin  $z = 0$  corresponds to the equator. Wave packets are generated at the equator and propagate away from it, while electrons rotate along the magnetic field with cyclotron frequencies. (b) One-dimensional system is used in the simulation. Variables  $z$  and  $B_0$  correspond to those in (a).

$$\Omega_e(z) = \Omega_{e0}(1 + az^2), \quad (2)$$

where  $\Omega_{e0}$  is the cyclotron frequency at the equator. We assumed the plasma frequency is constant in space, i.e.,  $\omega_{pe}(z) = \omega_{pe0}$ .

## III. NONLINEAR DYNAMICS OF RESONANT ELECTRONS

In this study, we assume that hiss waves propagate parallel to the background field. The linear dispersion relation of a whistler-mode wave is given by

$$c^2 k^2 = \omega^2 + \frac{\omega \omega_{pe}^2}{\Omega_e - \omega}, \quad (3)$$

where  $\omega$  and  $k$  are the frequency and wave number of the wave, respectively, and  $c$ ,  $\omega_{pe}$ , and  $\Omega_e$  represent the speed of light, the electron plasma frequency, and the electron cyclotron frequency, respectively. With dimensionless parameters  $\xi$  and  $\chi$  defined by  $\xi^2 = \omega(\Omega_e - \omega)/\omega_{pe}^2$  and  $\chi^2 = 1 - \omega^2/c^2 k^2$ , Eq. (3) is rewritten as follows:

$$\chi^2 = \frac{1}{1 + \xi^2}. \quad (4)$$

The phase velocity  $V_p$ , group velocity  $V_g$ , and resonance velocity  $V_R$  of the packet normalized by  $c$  can be obtained<sup>15</sup> as follows:

$$\tilde{V}_p = \frac{V_p}{c} = \chi \xi, \quad (5)$$

$$\tilde{V}_g = \frac{V_g}{c} = \frac{\xi}{\chi} \left\{ \xi^2 + \frac{\Omega_e}{2(\Omega_e - \omega)} \right\}^{-1}, \quad (6)$$

$$\tilde{V}_R = \frac{V_R}{c} = \chi \zeta \left( 1 - \frac{\Omega_e}{\gamma \omega} \right), \quad (7)$$

where  $\gamma$  is the Lorentz factor calculated by  $\gamma = 1/\sqrt{1 - v^2/c^2}$ , and  $v$  is the speed of an electron.

The motion of an electron interacting with a coherent whistler-mode wave is expressed by the pendulum equations, including an inhomogeneity factor  $S$ <sup>16,17</sup> as follows:

$$\frac{d\zeta}{dt} = \theta, \quad (8)$$

$$\frac{d\theta}{dt} = \omega_{tr}^2 (\sin \zeta + S), \quad (9)$$

where  $\theta = k(v_{\parallel} - V_R)$ . When  $v_{\parallel}$  approaches  $V_R$ ,  $\theta$  becomes 0. The parameter  $\zeta$  is the angle between the perpendicular velocity of the resonant electron  $v_{\perp}$  and the wave magnetic field  $B_w$ . The trapping frequency of resonant electrons  $\omega_{tr}$  is calculated by its trapping velocity  $V_{tr}$  as  $\omega_{tr} = kV_{tr} = \chi \sqrt{k v_{\perp} \Omega_w / \gamma}$ .

The inhomogeneity factor  $S$  has been used to evaluate the nonlinear resonance between electrons and waves.<sup>18</sup> It is calculated as follows:

$$S = -\frac{1}{s_0 \omega \Omega_w} \left( s_1 \frac{\partial \omega}{\partial t} + c s_2 \frac{\partial \Omega_e}{\partial h} \right), \quad (10)$$

where  $s_0 = \chi \tilde{v}_{\perp} / \zeta$ ,  $s_1 = \gamma(1 - \tilde{V}_R / \tilde{V}_g)^2$  and

$$s_2 = \frac{1}{2\zeta\chi} \left[ \frac{\gamma\omega}{\Omega_e} \tilde{v}_{\perp}^2 - \left( 2 + \frac{\chi^2(\Omega_e - \gamma\omega)}{\Omega_e - \omega} \right) \tilde{V}_R \tilde{V}_p \right]. \quad (11)$$

The normalized perpendicular velocity  $\tilde{v}_{\perp} = v_{\perp}/c$  is used in the equations. We will use the inhomogeneity factor  $S$  in Sec. VII to analyze the simulation results.

#### IV. NONLINEAR THEORY OF HISS GENERATION AND PROPAGATION

##### A. Wave generation

To model the observed dynamic spectra of the plasmaspheric hiss emissions reported in Ref. 8, we use the parameters specified in the paper as shown in Table I. First, the initial amplitudes of forward and backward propagating wave packets of hiss elements are designated at their generation points  $z_{gf}$  and  $z_{gb}$ , respectively, one by one at every constant period. We select  $50 \Omega_{e0}^{-1}$  for the time interval of the wave generation to avoid the large overlapping of packets. A frequency  $f_0$  is chosen for each packet in the range  $f_{\min} - f_{\max}$  from the random-like but deterministic series generated by a pseudo-random function.<sup>19</sup>

The amplitude of the packets is determined based on the nonlinear process of hiss generation. We understand that the hiss generation process is essentially the same as a chorus wave, which has been found to have a subpacket structure with a relatively short wave packet with frequency variation.<sup>20,21</sup> Additionally, a simulation study demonstrated a gradual transition from chorus emissions to hiss-like emissions due to variation of the background magnetic field inhomogeneity.<sup>22</sup> In this simulation, the optimum amplitude  $\Omega_{wo}$  and the threshold amplitude  $\Omega_{th}$  of the packet with the angular frequency  $\omega_0 = 2\pi f_0$  are calculated based on the nonlinear wave growth theory<sup>7,18</sup> as

TABLE I. Parameters used in the test particle simulations.

Parameter	Normalized value	Real value
Number of electrons $N_p$	1024	
Time step $\Delta t$	$0.02 / \Omega_{e0}$	$6.48 \times 10^{-7}$ s
Grid spacing $\Delta z$	$0.02 c / \Omega_{e0}$	194 m
System length $ z_{\max} $	$500c / \Omega_{e0}$	9.72 km
Cyclotron frequency at the equator $f_{ce}$		4909 Hz
$L$ value	4.8	
Plasma frequency $\omega_{pe}$	$23.3 \Omega_{e0}$	
Ratio of hot electrons $n_h/n_c$	$8 \times 10^{-5}$	
Frequency range of hiss $f_{\min} - f_{\max}$	$0.01 - 0.45 f_{ce}$	50–2200 Hz
Electron-hole depth $Q$	0.1	
Ratio of nonlinear transition time to trapping time $\tau$	0.5	
Velocity of electrons supporting waves $V_{\perp 0}$	$0.45c$	
Thermal momentum of electrons $U_{\parallel}$	$0.12c$	
Wave generation point (forward waves) $z_{gf}$	$-54.8 \Omega_{e0}/c$	$-1.0^\circ$ (latitude)
Wave generation point (backward waves) $z_{gb}$	$54.8 \Omega_{e0}/c$	$1.0^\circ$ (latitude)
Range of convective growth (forward waves)	$0 - 27.4 \Omega_{e0}/c$	$0^\circ - 0.5^\circ$ (latitude)
Range of convective growth (backward waves)	$-27.4 - 0 \Omega_{e0}/c$	$-0.5^\circ - 0^\circ$ (latitude)

$$\tilde{\Omega}_{wo} = \frac{\Omega_{wo}}{\Omega_{e0}} = 0.81\pi^{-5/2} \frac{|Q|}{\tau} \frac{s_1 \tilde{V}_g}{s_0 \tilde{\omega}_0 \tilde{U}_{\parallel}} \left( \frac{\chi \tilde{\omega}_{ph} \tilde{V}_{\perp 0}}{\gamma_w} \right)^2 \times \exp \left( -\frac{\gamma_w^2 \tilde{V}_R^2}{2 \tilde{U}_{\parallel}^2} \right), \quad (12)$$

$$\tilde{\Omega}_{th} = \frac{\Omega_{th}}{\Omega_{e0}} = \frac{100\pi^3 \gamma_w^3 \xi}{\tilde{\omega}_0 \tilde{\omega}_{ph}^4 \tilde{V}_{\perp 0}^5 \chi^5} \left( \frac{\tilde{a} s_2 \tilde{U}_{\parallel}}{Q} \right)^2 \exp \left( \frac{\gamma_w^2 \tilde{V}_R^2}{\tilde{U}_{\parallel}^2} \right), \quad (13)$$

respectively, where  $V_{\perp 0}$  is an averaged perpendicular velocity of hot electrons,  $U_{\parallel}$  is the thermal momentum in the parallel direction, and  $\omega_{ph}$  is the plasma frequency of hot electrons;  $\tilde{V}_{\perp 0} = V_{\perp 0}/c$  and  $\tilde{U}_{\parallel} = U_{\parallel}/c$  are the normalized parameters. The variables  $s_0$ ,  $s_1$ , and  $s_2$  are calculated with  $V_{\perp 0}$  and  $\gamma_w$  instead of  $v_{\perp}$  and  $\gamma$ ;  $\gamma_w = 1/\sqrt{1 - \tilde{V}_{\perp 0}^2 - \tilde{V}_R^2}$  is the Lorentz factor of the electrons supporting the wave; all variables in the equations introduced in Sec. IV are those of the electrons supporting the wave generation and growth, even though most of them are not denoted by the subscript  $w$ . The ratio  $\tau = T_N/T_{tr}$  determines the duration time of the packet generation  $T_N$ , where the nonlinear trapping time  $T_{tr} = 2\pi/\omega_{tr}$  is the period for trapped electrons to rotate once in the wave potential. The depth of the wave potential hole is represented by a dimensionless parameter  $Q$ .

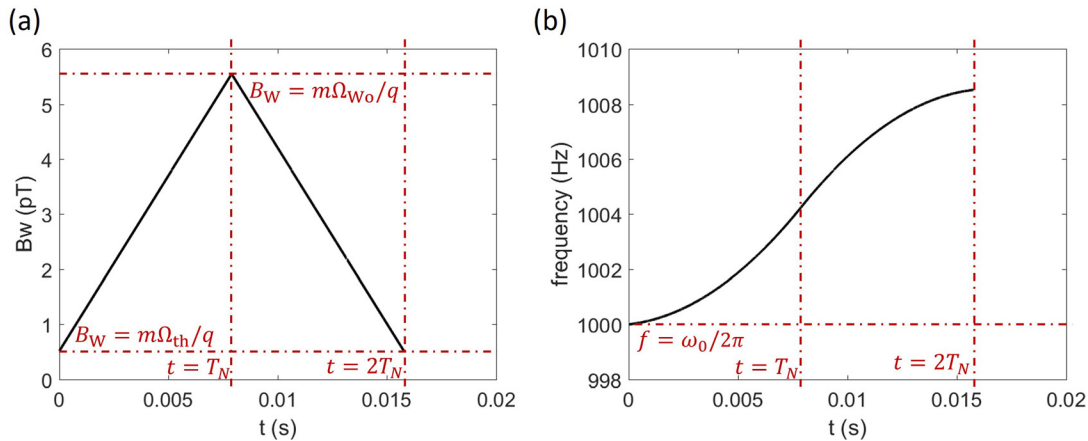


**FIG. 2.** Time evolution of (a) amplitude and (b) frequency of a wave packet with its initial frequency  $f_0 (= \omega_0/2\pi) = 1000$  Hz at the generation points  $z = z_{gf}, z_{gb}$ .

We express a wave amplitude  $B_w$  by  $\Omega_w = (q/m)B_w$  for comparison with the electron cyclotron frequency at the equator  $\Omega_{e0}$ , where  $q$  and  $m$  are the charge and mass of an electron, respectively. The normalized frequencies  $\tilde{\omega}_0 = \omega_0/\Omega_{e0}$  and  $\tilde{\omega}_{ph} = \omega_{ph}/\Omega_{e0}$  are used in the equation.

The time evolution of the packet amplitude  $\Omega_w$  at its generation point is modeled by a triangle wave. It is increased linearly from  $\Omega_w = \Omega_{th}$  to  $\Omega_{wo}$  for the generation time  $T_N$  and is linearly decreased from  $\Omega_{wo}$  to  $\Omega_{th}$  for another  $T_N$ . At the same time, the packet frequency  $\omega$  is increased from  $\omega_0$  with a frequency sweep rate<sup>23</sup>

$$\frac{\partial \tilde{\omega}}{\partial t} = \frac{2s_0}{5s_1} \tilde{\omega} \tilde{\Omega}_w. \quad (14)$$

Time evolutions of amplitude and frequency of a wave packet with  $f_0 (= \omega_0/2\pi) = 1000$  Hz are shown in Fig. 2 as an example.

### B. Separability criteria for coexistence of wave packets

Wave packets of hiss elements are generated near the equator through interaction with energetic electrons with temperature anisotropy.<sup>7</sup> Electromagnetic particle simulations<sup>9,10</sup> have demonstrated that many short wave packets of whistler-mode waves are simultaneously generated at different frequencies growing from thermal fluctuations because of positive linear growth rates in the lower frequency range and large nonlinear growth rates that work with coherent waves. The coherency of wave packets can be attained when the separability criteria described below are satisfied. A recent simulation study<sup>11</sup> shows that coherent wave packets grow from thermal fluctuations at discrete wave numbers and frequencies which satisfy the separability criteria.

Multiple wave packets can coexist at the same location with different frequencies. A motion of an electron is strongly modulated in the trapping regions of the waves.<sup>3</sup> The condition of an electron with its parallel velocity  $v_{\parallel}$  having resonances with the  $j$ th wave is represented by

$$V_R^j - V_{tr}^j < v_{\parallel} < V_R^j + V_{tr}^j, \quad (15)$$

where  $V_R^j$  is the resonance velocity of the  $j$ th wave, and  $V_{tr}^j$  is the widths of the trapping region in phase space. When the trapping

regions are sufficiently separated in phase space and have no overlaps, electrons can independently contribute to the generation of each packet without being disturbed by the other waves.

The condition for the independence of the wave packets can be expressed by the separability criterion:<sup>7</sup>

$$|V_R^{j+1} - V_R^j| \gg V_{tr}^j + V_{tr}^{j+1}. \quad (16)$$

Seed electrons that contribute to the packet generation need to satisfy this condition. The hiss structure consists of coherent whistler-mode waves satisfying the separability criterion.

The separability criterion (16) can be rewritten with the nonlinear trapping frequency as

$$|\omega^{j+1} - \omega^j| \gg \Delta\omega_w, \quad (17)$$

where the frequency bandwidth  $\Delta\omega_w$  is calculated by

$$\Delta\omega_w = 4\omega_{wtr} \left[ 1 + \frac{\chi^2}{\omega} \left( \frac{\Omega_e}{\gamma_w} - \omega \right) \left( \zeta^2 + \frac{\Omega_e}{2(\Omega_e - \omega)} \right) \right]^{-1}. \quad (18)$$

Here,  $\omega_{wtr} = \chi \sqrt{kV_{\perp 0} \Omega_w / \gamma_w}$  is the trapping frequency of the wave packet.

In the simulation, if the separability criterion is not satisfied with other packets, we discard the packet information with the frequency  $f_0$  and employ another frequency. This process is repeated until a new packet satisfying the separability criterion is found. A simplified criterion  $|\omega^{j+1} - \omega^j| > \Delta\omega_w$  can be used in the process because the interference of waves decreases exponentially with the frequency difference larger than  $\Delta\omega_w$ .<sup>24</sup> The packets' frequency gap needs to be slightly larger than  $\Delta\omega_w$ .

### C. Propagation of hiss elements

The generated forward and backward waves propagate away from the generation points to  $z_{max}$  and  $-z_{max}$ , respectively. The propagation of the wave packets with the group velocity  $V_g$  is determined by the equations

$$\frac{\partial \Omega_w}{\partial t} = -V_g \frac{\partial \Omega_w}{\partial z} + \Gamma_N \Omega_w, \quad (19)$$

$$\frac{\partial \omega}{\partial t} = -V_g \frac{\partial \omega}{\partial z}, \quad (20)$$

where we calculate the nonlinear growth rate  $\Gamma_N$  based on the nonlinear wave growth theory:<sup>18</sup>

$$\Gamma_N = \frac{|Q|\omega_{\text{ph}}^2}{2} \left( \frac{\xi}{\Omega_w \omega_0} \right)^{1/2} \frac{V_g}{U_{\parallel}} \left( \tilde{V}_{\perp 0} \frac{\chi}{\pi \gamma} \right)^{3/2} \exp \left( -\frac{\gamma^2 V_R^2}{2U_{\parallel}^2} \right). \quad (21)$$

We solve Eqs. (19) and (20) for each element using the first-order upwind difference method separately for forward and backward waves.

We select  $\Delta t$  satisfying  $\Delta t \Omega_{e0} \ll 1$  to properly follow the motions of electrons gyrating along the background magnetic field. In addition, we adopt  $\Delta z$  where  $\Delta z \gg V_g \Delta t$  is satisfied to avoid numerical errors in the wave propagation.

The convective growth rate  $\Gamma_N$  is calculated from an instantaneous amplitude at each time step and location by Eq. (21). Reference 8 found that the calculated amplitude becomes much larger than the observed amplitudes if the convective growth is assumed to take place in the whole latitude range. The paper also reported that if the convective growth occurs only in the latitudinal range of  $0^\circ$ – $0.5^\circ$ , the calculated amplitudes agree well with the observed ones. The possible reason for this finding is that the wave packets stop growing once the separability criteria are violated, as described in Sec. IV D. Hence, we follow the assumption and include the convective growth only between the limited space range shown in Table I.

We also calculate the wave phases of forward propagating waves by  $\psi$  from  $\psi = \omega t - kz$ , and those of backward waves by  $\psi = \omega t + kz$ , where  $k$  is obtained by the dispersion relation (3).

Figure 3 shows the analytical values of amplitudes and duration time calculated by Eqs. (12), (13), (20), and (21) with the parameters introduced in Table I. In Fig. 3(a), the red dashed line indicates the optimum amplitude calculated by Eq. (12) without taking the nonlinear wave growth into account. The threshold amplitude obtained by Eq. (13) crosses the optimum amplitude at 84 and 2287 Hz, which means the hiss waves can be generated and can grow only between the

frequencies. The blue solid line shows the optimum amplitude obtained by solving Eq. (20) with the convective growth rate Eq. (21). In this analytical calculation, the optimum amplitude becomes as high as 62 pT around 110 Hz. In the simulation, however, the rapid numerical damping owing to the triangle shape of the waves made the amplitudes no larger than 47 pT as the waves propagated, which can be confirmed in the spatial distribution of amplitude (Fig. 4) shown in Sec. IV D. The duration time of the hiss elements is longer for higher frequencies, as shown in Fig. 3(b).

### D. Produced hiss spectra

The method introduced in Sec. IV C produces wave packets shown in Figs. 4 and 5 in simulation. The spatial distribution of amplitudes at  $t = 0$  s is shown in Fig. 4. The packets of hiss elements are generated and propagate across the whole system. Figure 5 shows the time evolution of the amplitudes at a stationary point  $z = 27.4c/\Omega_{e0}$ . The enlargement of  $t = 0.6$ – $0.8$  s is shown in Fig. 5(b). Forward wave emissions with rising frequencies propagated in the positive  $z$  direction; hence, their frequencies decreased in space while increased in time.

The packet frequencies are shown by black solid lines in Fig. 6. Upper and lower separability criteria  $\Delta\omega_w$  are plotted in red and blue dashed lines, respectively. The dashed lines of the low-frequency ( $<1000$  Hz) packets did not overlap, which means the separability criterion is satisfied. Widths of  $\Delta\omega_w$  are narrower in lower frequencies, causing the higher density of the wave spectra. Packets with higher frequencies, on the other hand, have wider frequency intervals. Although the packets are adequately separated to satisfy the criterion at the equator, they experience significant convective growth, resulting in overlapping lines (violation of the criteria) in the off-equatorial region. It is expected in the actual phenomenon that convective growth stops so that the separability criterion is not violated. The latitude limitation of the convective growth assumed in Ref. 8 may be validated by the conservation of the separability criterion.

### V. TEST PARTICLE SIMULATION

The equations of motion are solved for 1024 electrons with initial values forming a delta functional distribution at an equatorial pitch angle  $\alpha_{\text{eq}0}$  and an energy  $E_0$ , where the subscript 0 denotes the initial

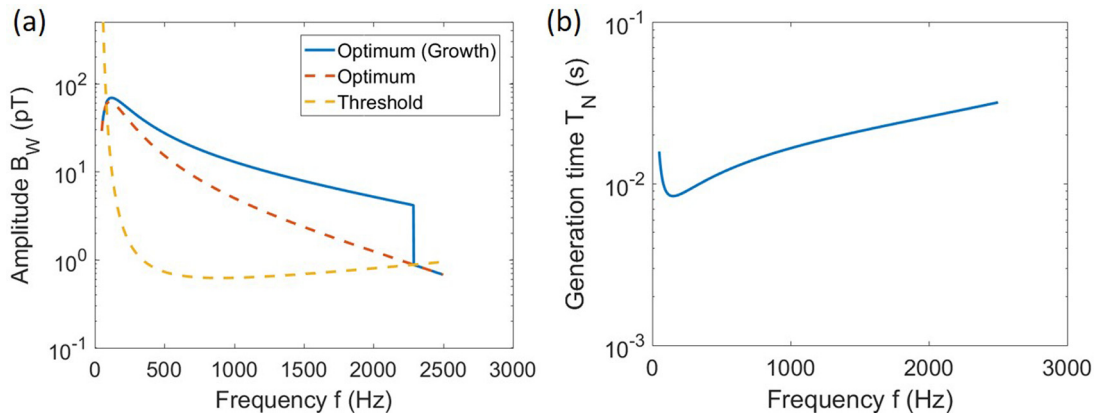


FIG. 3. (a) The frequency dependencies of the optimum amplitude with the convective growth (blue solid line) and without any growth (red dashed line) and the threshold amplitude (yellow dashed line). They are calculated by Eqs. (12), (13), and (21). (b) The generation time of the wave packets.

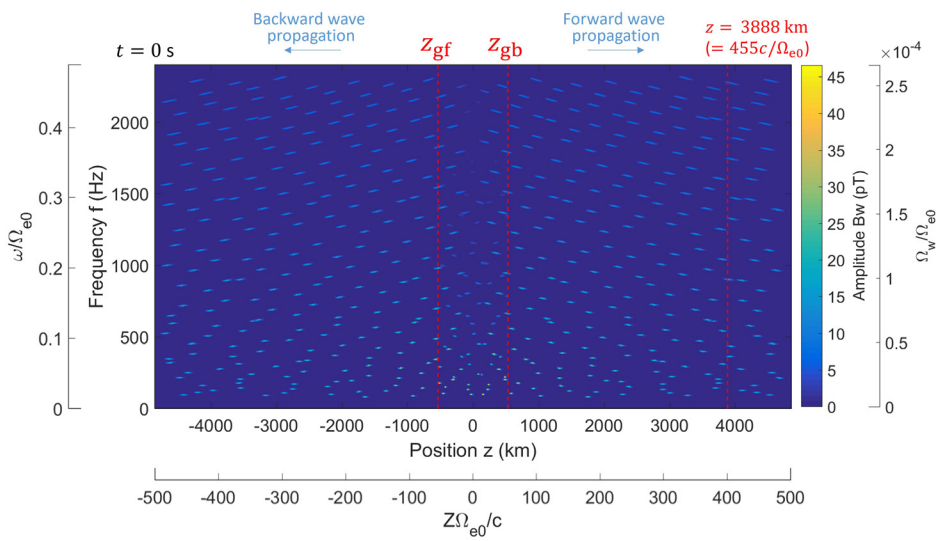


FIG. 4. The spatial distribution of amplitudes of wave packets produced in the simulation at  $t=0$ .

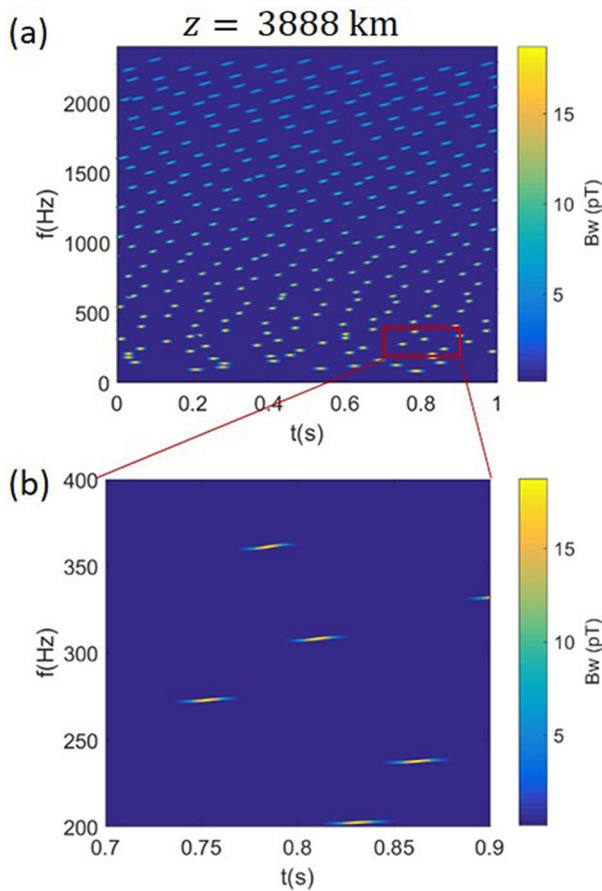


FIG. 5. (a) Frequency dynamic spectra of wave amplitude over  $t=0-1$  s at  $z = 455 c/\Omega_{e0}$ , and (b) its magnified figure between  $t=0.6-0.8$  s and  $f=200-400$  Hz.

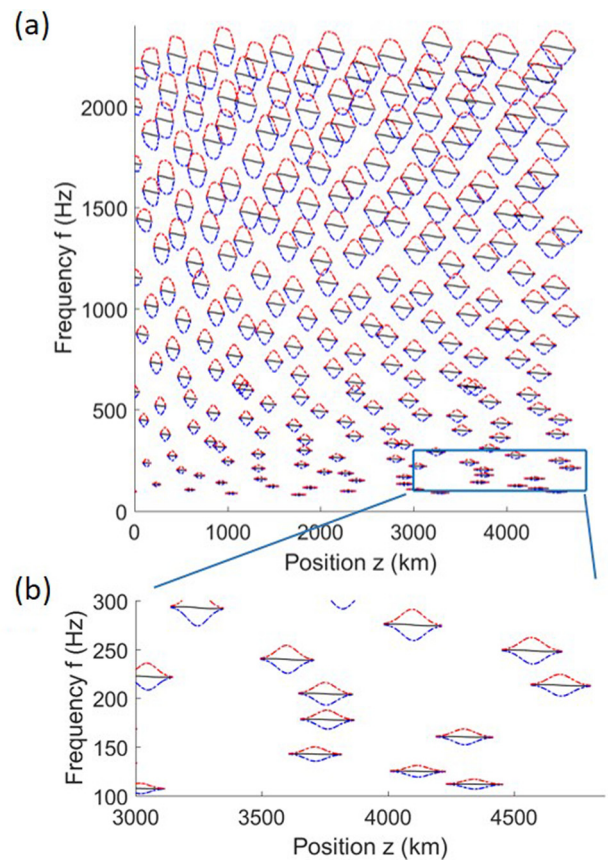


FIG. 6. (a) Spatial distribution of the packets' bandwidth in frequency and (b) its partly enlarged plot. The frequencies of the packets are plotted in black solid lines. Upper and lower limits of the frequency bandwidth  $\Delta\omega_w$  are denoted in red and blue dashed lines, respectively.

values of the electrons. The gyrophases of the electrons are uniformly distributed over the range  $\phi = 0-2\pi$ . Initial locations of electrons are at  $z = 0$ , and their directions with a parallel velocity  $v_{\parallel}$  are positive for the half number of electrons and negative for the others.

To evaluate the effect of waves fully distributed across the frequency range and the system length, we first calculate the wave propagations without solving the motion of electrons at the beginning of the simulation. We define the time as  $t = 0$  after the wave packets fill the entire space, as shown in Fig. 4 and then we start solving the motion of electrons. The amplitudes and frequencies of the wave packets are linearly interpolated in space to obtain the values at the locations of the electrons. We employ the same time step for updating waves and computing the electron trajectories; hence, the interpolation in time is not needed.

## VI. NUMERICAL RESULTS

### A. Diffusion coefficient of pitch angle and momentum

We quantitatively evaluate the scattering of electrons by introducing nonlinear diffusion coefficients. A diffusion coefficient  $D$  of particles scattered in time  $T$  is generally calculated by  $D = \sigma^2/2T$ , where  $\sigma$  is a standard deviation. We define a nonlinear diffusion coefficient of the equatorial pitch angle<sup>25,26</sup> by

$$D_x = \frac{\sigma_x^2}{2T} = \frac{1}{2TN_p} \sum_{i=1}^{N_p} (\alpha_{eqi} - \bar{\alpha})^2, \quad (22)$$

where  $N_p$  is the number of particles. An average of their equatorial pitch angles  $\bar{\alpha}_{eq}$  is obtained by  $\bar{\alpha}_{eq} = \sum_{i=1}^{N_p} \alpha_{eqi}/N_p$ .

The coefficients  $D_v$  and  $D_p$  are similarly defined to evaluate the diffusion in velocity and momentum, respectively, as

$$\frac{D_v}{c^2} = \frac{1}{2Tc^2N_p} \sum_{i=1}^{N_p} (v_i - \bar{v})^2, \quad (23)$$

$$\frac{D_p}{p_0^2} = \frac{1}{2Tp_0^2N_p} \sum_{i=1}^{N_p} (p_i - \bar{p})^2, \quad (24)$$

where  $p = \gamma mv$  is a relativistic momentum of an electron, whose initial value is  $p_0$ , and  $m$  is the electron rest mass. The average velocity  $\bar{v}$  and the average momentum  $\bar{p}$  are calculated by  $\bar{v} = \sum_{i=1}^{N_p} v_i/N_p$  and  $\bar{p} = \sum_{i=1}^{N_p} p_i/N_p$ , respectively.

Tracing trajectories of electrons over  $T = 1.62$  s with different initial values of equatorial pitch angle and energy, we calculate  $D_x$  as shown in Fig. 7(a). The high values of  $D_x$  are observed for the electrons with mid-to-high pitch angle and energy ( $\alpha_{eq0} \geq 40^\circ$ ,  $E_0 < 2$  MeV), especially in the range of mid-pitch angle and low energy ( $40^\circ \leq \alpha_{eq0} < 80^\circ$ ,  $E_0 \leq 20$  keV), while they are limited to moderate values for electrons with high pitch angle and high energy ( $\alpha_{eq0} \geq 80^\circ$ ,  $E_0 \geq 2$  MeV). We note that the mirror points of the electrons are outside the simulation system for  $\alpha_{eq0} \leq 75^\circ$  when  $E_0 < 510$  keV. The lapse time outside the system is not taken into account; hence, the diffusion coefficient is overestimated in those conditions, where a complete simulation will be in the scope of a future study. On the other hand, the mirror points are inside the system when  $E_0 \geq 510$  keV, or  $\alpha_{eq0} > 75^\circ$  for  $E_0 < 510$  keV, and the diffusion coefficients are correctly computed. Those are the conditions

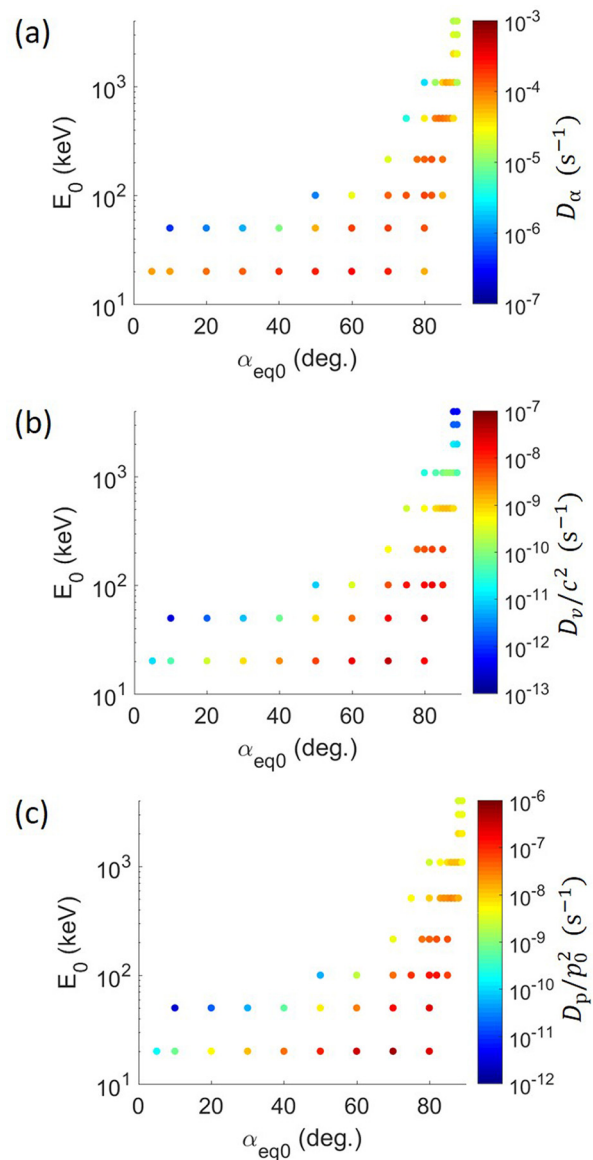


**FIG. 7.** Simulation results of the nonlinear diffusion coefficients (a)  $D_x$ , (b)  $D_v/c^2$ , and (c)  $D_p/p_0^2$  for  $\alpha_{eq0} = 5^\circ-89^\circ$  and  $E_0 = 15-4000$  keV. The cases satisfying the first-order resonance are mainly plotted.

where the nonlinear wave-particle interaction is expected, as described in Sec. VII.

The line plots of the diffusion coefficient with specific energies are shown in Fig. 8. The maximum point of the pitch angle diffusion coefficient  $D_x$  shifted to a higher pitch angle as the initial energy increased.

The coefficients  $D_v/c^2$  and  $D_p/p_0^2$  calculated by Eqs. (23) and (24) are shown in Figs. 7(b) and 7(c), respectively. The diffusion coefficients in energy are much smaller than those in pitch angles. The large diffusion is observed in the region of  $\alpha_{eq0} > 40^\circ$  and  $E_0 \leq 1$  MeV, while the moderate diffusion is seen in  $E_0 > 1$  MeV.

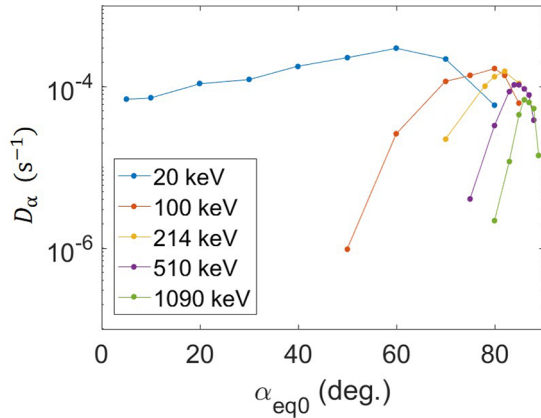


**FIG. 8.** Pitch angle diffusion coefficient  $D_\alpha$  as a function of initial equatorial pitch angles  $\alpha_{eq0}$  for initial energies  $E_0 = 20, 100, 214, 510,$  and  $1090$  keV.

**B. Particle distribution function and trajectories of electrons**

Figure 9 shows the particle distribution functions of the injected electrons with six initial conditions;  $f(\alpha_{eq})$  (the first and third columns) and  $f(E)$  (the second and fourth columns) are the particle distribution functions of the equatorial pitch angle and energy, respectively, plotted on the log scale.

The Gaussian-like distribution is observed in Fig. 9(e) ( $\alpha_{eq0}, E_0 = (60^\circ, 100$  keV) (in the range of mid-pitch angle and mid-energy), which indicates that the particles experience a diffusive process. The nonlinear diffusion coefficients are generally of the same order of magnitude as the QL diffusion coefficients, as discussed in Sec. VII.

On the other hand, non-diffusive processes are observed for  $E_0 = 20$  keV (in the low-energy range) and  $\alpha_{eq0} =$  (a)  $5^\circ$ , (b)  $10^\circ$ , and (c)  $80^\circ$  in Fig. 9. The distribution shifts to a lower pitch angle in (c). The distributions especially show non-Gaussian shapes in (a) and (b).

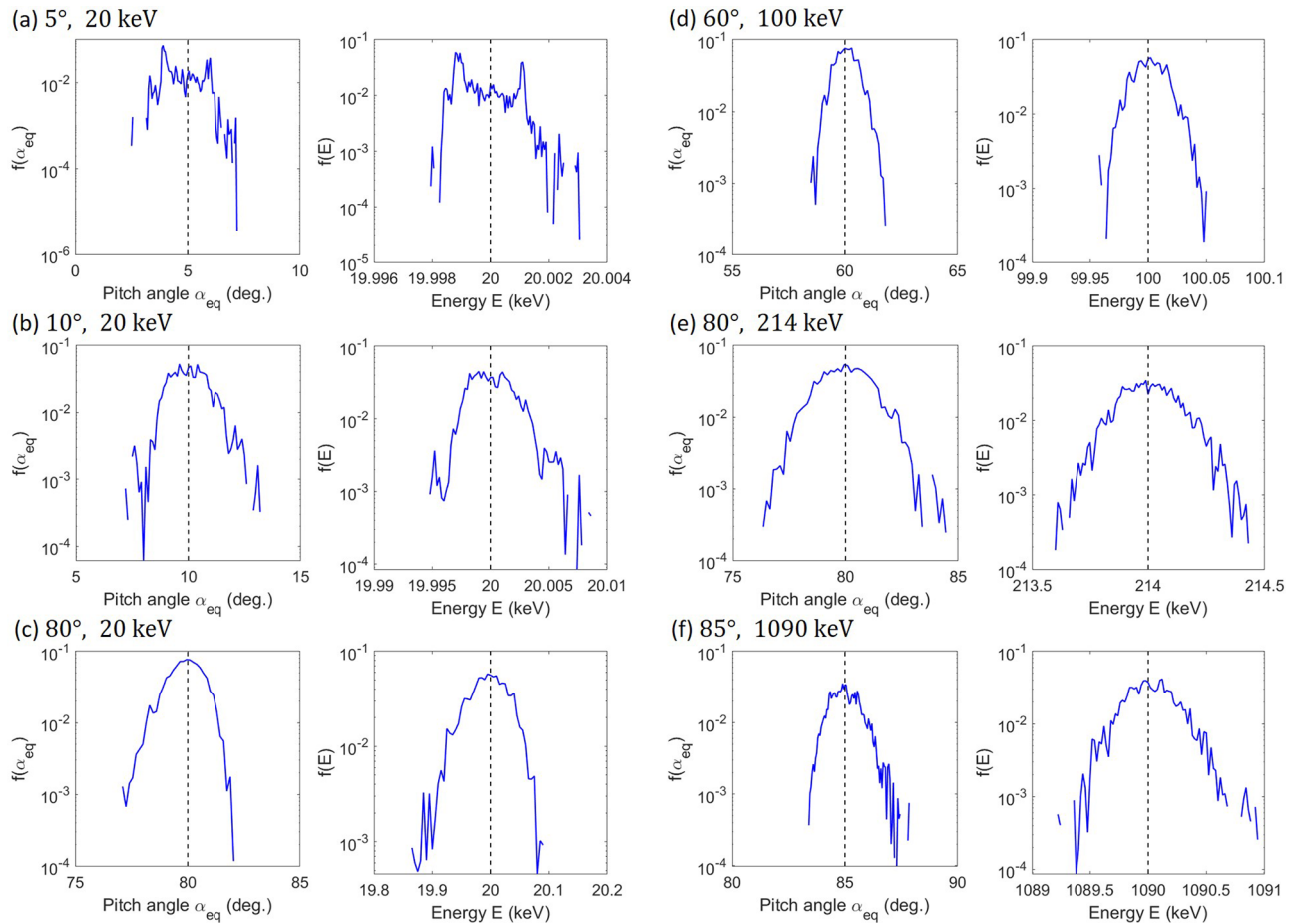


**FIG. 9.** Particle distribution functions of the equatorial pitch angle (the first and third columns) and energy (the second and fourth columns) formed by injected electrons. The initial conditions  $\alpha_{eq0}, E_0$  are (a)  $5^\circ, 20$  keV, (b)  $10^\circ, 20$  keV, (c)  $80^\circ, 20$  keV, (d)  $60^\circ, 100$  keV, (e)  $80^\circ, 214$  keV, and (f)  $85^\circ, 1090$  keV. The black dashed line in the center corresponds to the initial condition given by the delta function.

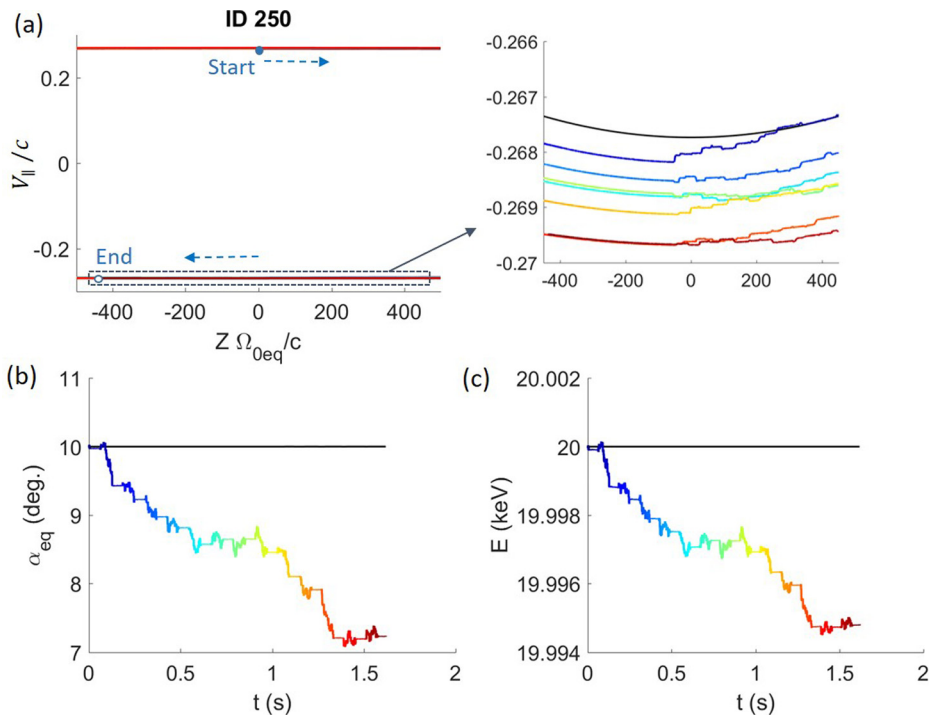


**FIG. 10.** (a) The trajectory of the particle which had the lowest pitch angle at  $t = 1.62$  s is shown in the  $z-v_{||}$  plane. The initial conditions of pitch angle and energy are  $\alpha_{eq0} = 20^\circ$  and  $E_0 = 20$  keV, respectively. Time variations of (b) pitch angle and (c) kinetic energy of the electron are also shown in the same color. The black solid line in the figures indicates the correspondence of adiabatic electrons.

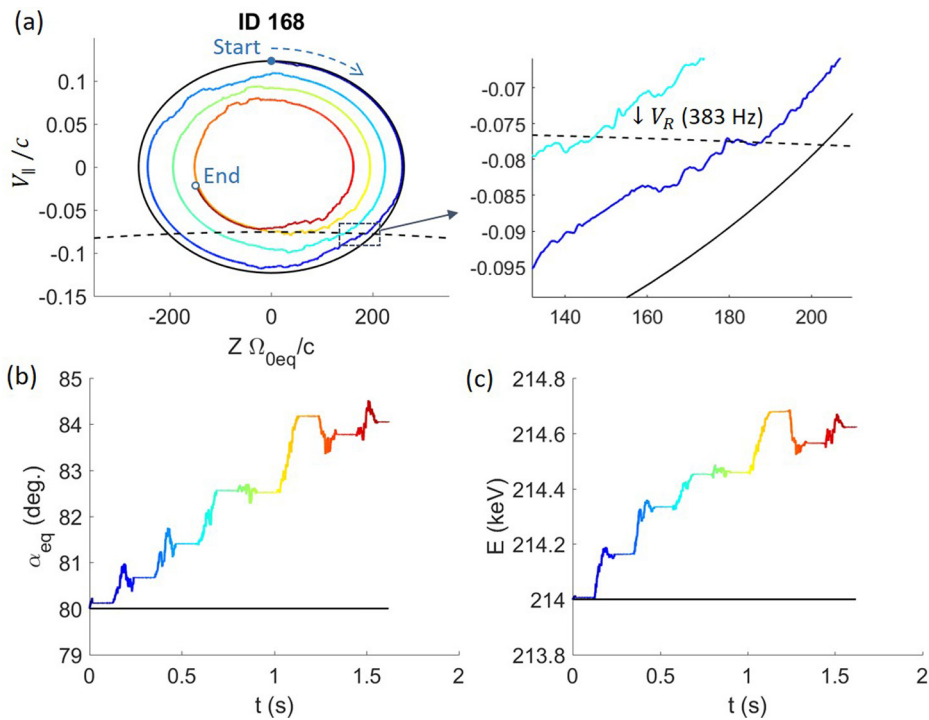


**FIG. 11.** (a) The trajectory of the particle which had the highest pitch angle at  $t = 1.62$  s is shown in the  $z-v_{||}$  plane. The initial conditions of pitch angle and energy are  $\alpha_{eq0} = 80^\circ$  and  $E_0 = 214$  keV, respectively. Time variations of (b) pitch angle and (c) kinetic energy of the electron are also shown in the same color. The black solid line in this figure indicates the correspondence of adiabatic electrons.

The distribution is shifted to the low-pitch-angle region in (a), while a shift to a higher pitch angle is observed in (b). This result can be attributed to the anomalous trapping often observed in the low-pitch-angle region.<sup>27</sup> The anomalous trapping can occur when

$$\left(\frac{\Omega_w}{\Omega_e}\right)^{0.5} \sim \left(\frac{v_{\perp}}{V_p - V_R}\right)^{1.5} \quad (25)$$

is satisfied.<sup>18</sup> It is confirmed that the condition is generally satisfied below 15° in pitch angle and 25 keV in energy in this simulation.

As can be observed in Fig. 9(b), a small part of the particles experience a sudden decrease in pitch angle and form a bump in the low-pitch-angle region, which indicates a part of the particles can precipitate into loss cones faster than the estimation by the Gaussian diffusion.

Figure 10(a) shows the trajectory of the particle whose resultant pitch angle is the lowest when the initial equatorial pitch angle and energy are 10° and 20 keV, respectively. The enlargement in the negative parallel velocity is shown on the right of (a). The black solid line indicates the adiabatic motion, which is supposed to be circular, but the motion outside the spatial limitation of the system is not

calculated; hence, only the upper and lower parts of the trajectory are shown. The electron goes through resonances with multiple waves and is gradually deviated from the adiabatic trajectory toward the outside. The corresponding time evolutions of pitch angle and energy are shown in Figs. 10(b) and 10(c). The particle loses energy as it is precipitated to a lower pitch angle.

Non-diffusive acceleration is also observed in Figs. 9(e) 80°, 214 keV and 9(f) 85°, 1090 keV, which are in the range of high pitch angle and mid-energy. We observe bumps in the right part of the distribution functions, especially in  $f(\alpha_{eq})$  of (e), which means a part of particles experiences effective acceleration; this is considered to be caused by nonlinear trappings. To illustrate the nonlinear wave-particle interaction observed in Fig. 9(e), the trajectory of the particle, which shows the largest pitch angle increase of the 1024 particles, is shown in Fig. 11(a). The enlarged figure is shown on the right side. The particle is accelerated by successive nonlinear trappings and moves along the wave resonance lines for a short time. The particle follows the 383-Hz resonance line for 3 ms, corresponding to about 15 gyroperiods, which is considered to be the trapping by the wave.

Figure 12 shows the two-dimensional plots of the distribution of particles with initial conditions used in Fig. 9. White dashed lines

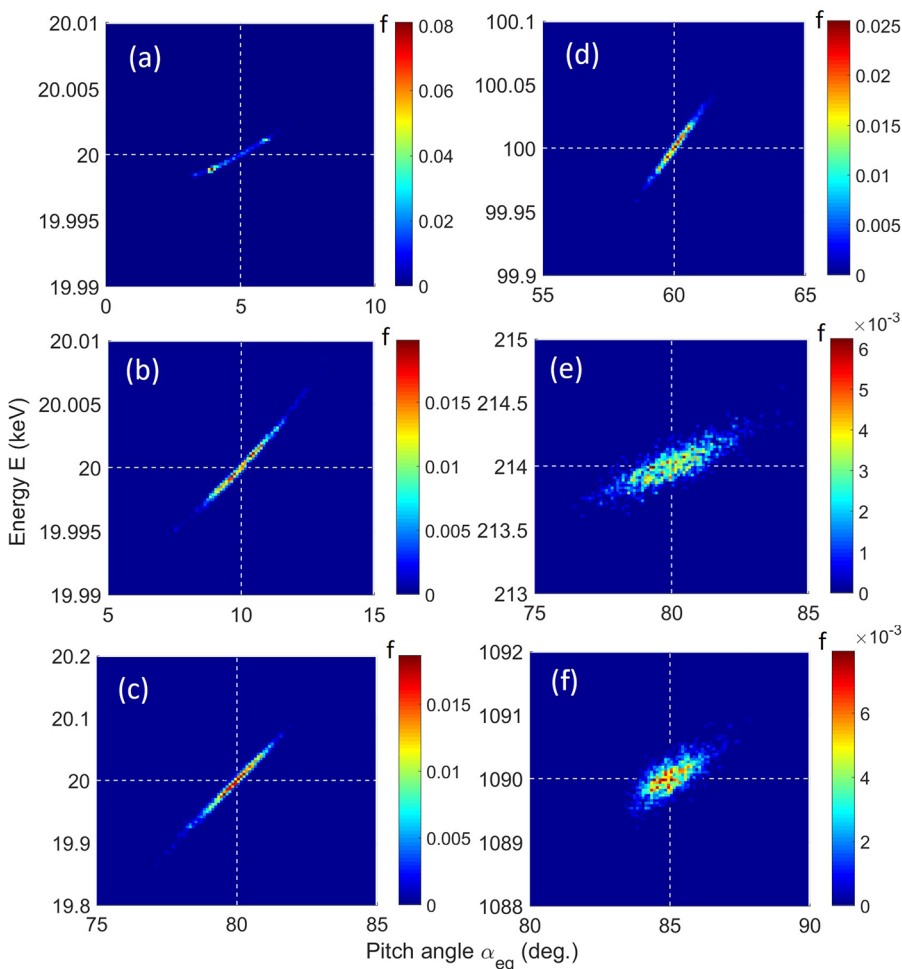
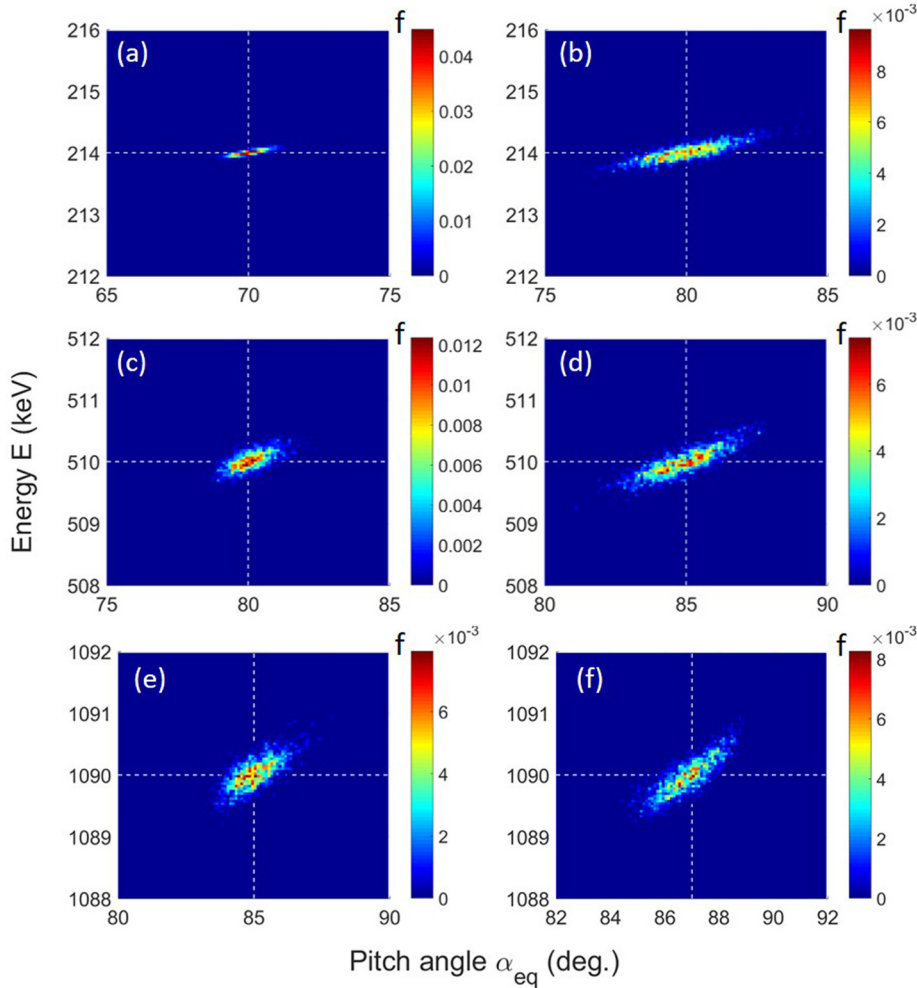


FIG. 12. Two-dimensional plots of the particle distribution functions with the identical initial conditions used in Fig. 9. White dashed lines indicate the initial equatorial pitch angles and energies. The crossing point of the lines corresponds to the initial condition given by the delta function.



**FIG. 13.** Two-dimensional plots of the particle distribution functions with various initial conditions. The initial equatorial pitch angles and energies ( $\alpha_{eq0}, E_0$ ) are (a) ( $70^\circ, 214$  keV), (b) ( $80^\circ, 214$  keV), (c) ( $80^\circ, 510$  keV), (d) ( $85^\circ, 510$  keV), (e) ( $85^\circ, 1090$  keV), and (f) ( $87^\circ, 1090$  keV). White dashed lines indicate the initial equatorial pitch angles and energies. Crossing points of the lines correspond to the initial conditions given by the delta function.

show the initial equatorial pitch angles and energies. Crossing points of the lines denote the initial conditions given by the delta function. Positive correlations between pitch angle and energy variations are observed in all cases. For the sake of providing more comprehensive information, the two-dimensional particle distribution functions with various initial conditions are plotted in Fig. 13. Here, we can also observe positive correlations with every energy and pitch angle.

**VII. DISCUSSION**

In the nonlinear wave–particle interaction with a coherent wave potential, the scattering of resonant electrons depends on the inhomogeneity factor  $S$  computed by Eq. (10). Resonant electrons going through the wave potentials are thermalized effectively when  $S$  is around one or smaller. The maximum thermalization takes place with  $|S| = 1$  even though trapping does not occur with that condition.<sup>24</sup>

The dependence of the nonlinear thermalization  $\Delta V_t^2$  on the inhomogeneity factor  $S$  obtained from Fig. 7 of Ref. 24 is plotted by dots in Fig. 14(a). They are normalized by the value at  $|S| = 1$ . We approximated the result by an equation

$$g(S) = |S|^a \exp[-a(|S| - 1)] \tag{26}$$

with  $a = 8$ , which is plotted by a dashed line in Fig. 14(a). It is predicted that the larger the value of  $g(S)$ , the greater the effect of thermalization on diffusion.

The largest  $g(S)$  in the whole system space in the frequency range 50–2200 Hz is shown in Fig. 14(b). Here,  $S$  is calculated by Eq. (10) with the variables  $\gamma$  and  $v_\perp$  of the tested electrons, which do not contribute to the packet generation. The maximum amplitude  $m\Omega_{wo}/q$  is used as an amplitude whose spatial distribution is obtained by solving Eqs. (19) and (20) for the frequencies from 100 to 2300 Hz with an interval of 100 Hz. The amplitude of the in-between frequencies is calculated by linear interpolation. The value of  $g(S)$  is almost zero in the range of  $\alpha_{eq0} \leq 60^\circ$  and  $E_0 \leq 20$  keV; hence, the particles are not expected to have effective nonlinear interaction with waves. The result can explain that the diffusion coefficients obtained by the nonlinear simulation reasonably agree with those calculated by the QL theory, as discussed in this section. Particles with the mid-to-high pitch angle ( $\alpha_{eq0} > 60^\circ$ ) and mid-to-high energy ( $E_0 > 20$  keV) show high values of  $g(S)$ ; therefore, they are supposed to experience effective

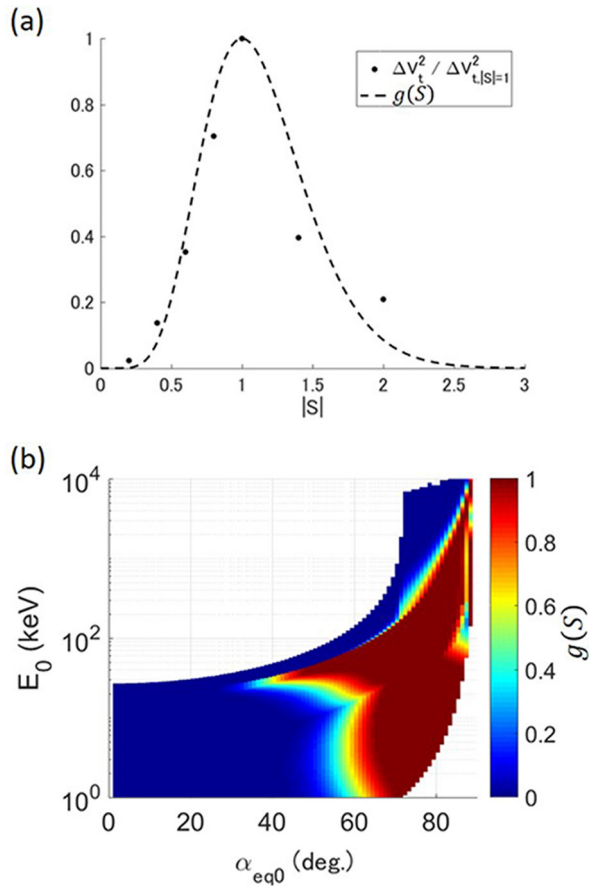


**FIG. 14.** In the nonlinear interaction with a coherent wave potential, the scattering of resonant electrons depends on the inhomogeneity factor  $S$ . (a) The dependence of nonlinear thermalization  $\Delta V_t^2$  on the inhomogeneity factor  $S$  obtained from Fig. 7 of Ref. 24 is plotted by dots. They are normalized by the value at  $|S| = 1$ . Approximated function  $g(S)$  with  $a = 8$  is denoted by a dashed line. It is predicted that the larger the value of  $g(S)$ , the greater the thermalization effect on diffusion. (b) The largest  $g(S)$  over all the system space in the frequency range 50–2200 Hz is shown. Specific frequencies are excluded when the threshold amplitude is larger than the optimum amplitude.

thermalization during the nonlinear wave–particle interaction; we actually observed bumps of the distribution function by the non-diffusive acceleration in Figs. 9(e) and 9(f), and a long resonance of a particle with a wave packet in Fig. 11. However, their diffusion coefficients are not very high according to Fig. 7; the diffusion coefficients are especially low in the high-pitch-angle and high-energy range ( $\alpha_{eq0} \geq 80^\circ$ ,  $E_0 > 2$  MeV). This result may be explained by another factor related to wave separation and overlaps, as described below.

The ratio of  $\Delta\omega_p$  to  $\Delta\omega_w$  can be used as an index of the packet separation seen from the energetic electrons. The parameter  $\Delta\omega_w$  introduced in Eq. (18) is a packet bandwidth calculated from the properties of electrons supporting the wave generation and growth.<sup>24</sup> As described in Sec. IV B, according to the separability criteria, the frequency separation of the wave packets needs to be larger than  $\Delta\omega_w$  for the wave generation or the waves cannot be generated in the first place.

To satisfy this criterion, we adjust the frequency separation to be larger or almost equal to  $\Delta\omega_w$  through all frequency ranges in our simulation (see Fig. 6). Therefore, the packet bandwidth  $\Delta\omega_w$  can be considered as an indication of the frequency interval between the wave packets.

The parameter  $\Delta\omega_p$  represents the packet bandwidth seen from the tested electrons. It is basically calculated by Eq. (18), but the parameters are replaced with those of the specific resonant electrons that are not responsible for the packet generation; specifically,  $\gamma_w$  and  $\omega_{wtr}$  are replaced with  $\gamma$  and  $\omega_{tr}$ , respectively. The tested electrons are assumed to have the same energy  $E$  and pitch angle  $\alpha_{eq}$  used in the nonlinear test particle simulation.

When the ratio  $\Delta\omega_p/\Delta\omega_w$  is larger than unity, the bandwidth experienced by tested electrons becomes larger than the actual frequency separation of the wave packets. Therefore, the tested electrons behave as if they undergo resonances with multiple overlapped waves, which causes a chaotic motion instead of nonlinear trapping. The ratio  $\Delta\omega_p/\Delta\omega_w$  corresponds to the inverse value of  $d$ , which was introduced in Ref. 24 as a normalized distance between two waves in velocity space. The ratio corresponds to the resonance-overlap parameter of the Chirikov overlap criterion.<sup>28,29</sup>

The obtained result of  $\Delta\omega_p/\Delta\omega_w$  is shown in Fig. 15. For electrons with low pitch angle and low energy,  $\Delta\omega_p/\Delta\omega_w$  is far lower than 1, which means potentials are separated enough to satisfy the separability criteria. In such cases, nonlinear particle resonance can occur independently in each wave. In the high-pitch-angle range of high-energy electrons (1–2 MeV), on the other hand, there occurs overlapping of nonlinear trapping potentials resulting in a reduction of the efficiency of the coherent nonlinear trapping effect. The overlapping causes the chaotic motion of resonant electrons, making the nonlinear scattering less effective. This fact could explain why the diffusion coefficient of high-pitch-angle and high-energy electrons remains low.

The calculations of the pitch angle diffusion coefficient  $D_{\alpha\alpha}$  by the QL theory have been widely conducted.<sup>2,30–32</sup> We compare the diffusion rates due to nonlinear wave–particle interaction with those by the QL theory. The maximum wave amplitudes of the present model in midlatitude are about 20 pT, as shown in Fig. 5, which corresponds to the low magnetic activity assumed in Figs. 8 and 9 of Ref. 2. We find a good agreement between  $D_{\alpha\alpha}$  and  $D_{\alpha}$  calculated in the present simulation. Both of them are about  $10^{-4} \text{ s}^{-1}$ . It is interesting that the diffusion rates are of the same order of magnitude despite the distinct difference between the nonlinear and the QL diffusion models. The process of pitch angle scattering by the coherent waves is properly represented by the QL theory, except for the acceleration effect due to nonlinear trapping, as discussed above.

## VIII. CONCLUSIONS

Scattering of energetic electrons by plasmaspheric hiss was studied by nonlinear test particle simulation. Several hundred hiss packets, which adequately satisfied the separability criterion, were independently calculated based on the nonlinear theory of hiss generation and propagation. We observed the trapping of particles, which is nonlinear wave–particle interaction. The scattering of electrons was quantitatively evaluated by diffusion coefficients of pitch angle, velocity, and momentum. The thermalization seemed to be determined by two factors: the inhomogeneity factor  $S$  and an index of packet separation  $\Delta\omega_p/\Delta\omega_w$ . The diffusion coefficients obtained by the nonlinear simulation were of the same order of magnitude as those calculated by the

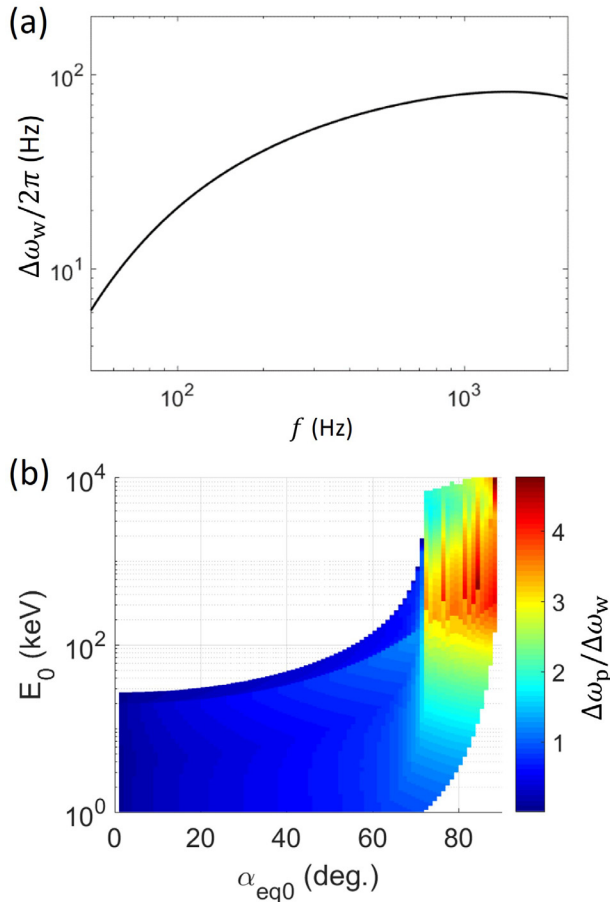


**FIG. 15.** (a) Frequency bandwidth  $\Delta\omega_w$  calculated from the energy of electrons generating the hiss emissions. Parameters at the generation point of the packets are used. (b) Maximum  $\Delta\omega_p/\Delta\omega_w$  over all the system space range.  $\Delta\omega_p$  is the bandwidth calculated from each initial energy  $E_0$  of electrons independent of the wave generation. The ratio  $\Delta\omega_p/\Delta\omega_w$  represents the degree of bandwidth overlap between two waves. Packet frequencies are chosen from the range 50–2200 Hz, excluding those whose threshold amplitudes are larger than their optimum amplitudes.

QL theory. Compared with the diffusion estimated by the QL theory, a small portion of the resonant particles experienced more rapid acceleration because of the wave trapping or quicker precipitation due to the nonlinear resonance with the coherent waves.

Only parallel propagation was considered in the present study. However, there can be a strong influence of Landau resonance by oblique propagations, especially for low energies below 10 keV or high pitch angles above  $85^\circ$ .<sup>32–35</sup> The interaction between obliquely propagating hiss elements and electrons will be studied in the future.

## ACKNOWLEDGMENTS

The test particle simulations in the present study were conducted on the KDK computer system at Research Institute for Sustainable Humanosphere, Kyoto University. This work was supported by JSPS KAKENHI Grant No. JP17H06140.

## AUTHOR DECLARATIONS

### Conflict of Interest

The authors have no conflicts to disclose.

### Author Contributions

**Miwa Tobita:** Conceptualization (equal); Data curation (equal); Formal analysis (equal); Methodology (equal); Visualization (equal); Writing – original draft (equal); Writing – review & editing (equal). **Yoshiharu Omura:** Conceptualization (equal); Funding acquisition (equal); Methodology (equal); Supervision (equal); Writing – original draft (equal); Writing – review & editing (equal).

## DATA AVAILABILITY

The data that support the findings of this study are available from the corresponding author upon reasonable request.

## REFERENCES

- <sup>1</sup>D. Summers, B. Ni, and N. P. Meredith, *J. Geophys. Res.: Space Phys.* **112**, A04206, <https://doi.org/10.1029/2006JA011801> (2007).
- <sup>2</sup>D. Summers, B. Ni, and N. P. Meredith, *J. Geophys. Res.: Space Phys.* **112**, A04207, <https://doi.org/10.1029/2006JA011993> (2007).
- <sup>3</sup>Y. Omura, D. Nunn, H. Matsumoto, and M. J. Rycroft, *J. Atmos. Terr. Phys.* **53**, 351 (1991).
- <sup>4</sup>D. Shklyar and H. Matsumoto, *Surv. Geophys.* **30**, 55 (2009).
- <sup>5</sup>O. Allanson, C. E. J. Watt, H. Ratcliffe, H. J. Allison, N. P. Meredith, S. N. Bentley, J. P. J. Ross, and S. A. Glauert, *J. Geophys. Res.: Space Phys.* **125**, e2020JA027949, <https://doi.org/10.1029/2020JA027949> (2020).
- <sup>6</sup>D. Summers, Y. Omura, S. Nakamura, and C. A. Kletzing, *J. Geophys. Res.: Space Phys.* **119**, 9134, <https://doi.org/10.1002/2014JA020437> (2014).
- <sup>7</sup>Y. Omura, S. Nakamura, C. A. Kletzing, D. Summers, and M. Hikishima, *J. Geophys. Res.: Space Phys.* **120**, 7642, <https://doi.org/10.1002/2015JA021520> (2015).
- <sup>8</sup>S. Nakamura, Y. Omura, D. Summers, and C. A. Kletzing, *Geophys. Res. Lett.* **43**, 10040, <https://doi.org/10.1002/2016GL070333> (2016).
- <sup>9</sup>M. Hikishima, Y. Omura, and D. Summers, *J. Geophys. Res.: Space Phys.* **125**, e2020JA027973, <https://doi.org/10.1029/2020JA027973> (2020).
- <sup>10</sup>Y. Liu, Y. Omura, and M. Hikishima, *Earth, Planets Space* **73**, 230 (2021).
- <sup>11</sup>Y. Liu and Y. Omura, *J. Geophys. Res.: Space Phys.* **127**, e2022JA030428, <https://doi.org/10.1029/2022JA030428> (2022).
- <sup>12</sup>X. Tao, J. Bortnik, J. M. Albert, R. M. Thorne, and W. Li, *J. Geophys. Res.: Space Phys.* **119**, 8848, <https://doi.org/10.1002/2014JA020022> (2014).
- <sup>13</sup>L. Gan, W. Li, Q. Ma, A. V. Artemyev, and J. M. Albert, *J. Geophys. Res.: Space Phys.* **127**, e2021JA030063, <https://doi.org/10.1029/2021JA030063> (2022).
- <sup>14</sup>L. Gan, W. Li, Q. Ma, J. M. Albert, and A. V. Artemyev, *Geophys. Res. Lett.* **47**, e2019GL085987, <https://doi.org/10.1029/2019GL085987> (2020).
- <sup>15</sup>Y. Omura, Y. Katoh, and D. Summers, *J. Geophys. Res.: Space Phys.* **113**, A04223, <https://doi.org/10.1029/2007JA012622> (2008).
- <sup>16</sup>D. Nunn, *Planet. Space Sci.* **22**, 349 (1974).
- <sup>17</sup>V. I. Karpman, J. N. Istomin, and D. R. Shklyar, *Phys. Scr.* **11**, 278 (1975).
- <sup>18</sup>Y. Omura, *Earth, Planets Space* **73**, 95 (2021).
- <sup>19</sup>C. K. Birdsall and A. B. Langdon, *Plasma Physics via Computer Simulation* (CRC Press, 1985).
- <sup>20</sup>O. Santolík, C. A. Kletzing, W. S. Kurth, G. B. Hospodarsky, and S. R. Bounds, *Geophys. Res. Lett.* **41**, 293, <https://doi.org/10.1002/2013GL058889> (2014).
- <sup>21</sup>J. C. Foster, P. J. Erickson, Y. Omura, D. N. Baker, C. A. Kletzing, and S. G. Claudepierre, *J. Geophys. Res.: Space Phys.* **122**, 324, <https://doi.org/10.1002/2016JA023429> (2017).
- <sup>22</sup>Y. Katoh and Y. Omura, *J. Geophys. Res.: Space Phys.* **118**, 4189, <https://doi.org/10.1002/jgra.50395> (2013).
- <sup>23</sup>Y. Omura, M. Hikishima, Y. Katoh, D. Summers, and S. Yagitani, *J. Geophys. Res.: Space Phys.* **114**, A07217, <https://doi.org/10.1029/2009JA014206> (2009).

- <sup>24</sup>M. Tobita and Y. Omura, *Phys. Plasmas* **25**, 032105 (2018).
- <sup>25</sup>C. F. Kennel and H. E. Petschek, *J. Geophys. Res.* **71**, 1, <https://doi.org/10.1029/JZ071i001p00001> (1966).
- <sup>26</sup>G. S. Lakhina, B. T. Tsurutani, O. P. Verkhoglyadova, and J. S. Pickett, *J. Geophys. Res.: Space Phys.* **115**, A00F15, <https://doi.org/10.1029/2009JA014885> (2010).
- <sup>27</sup>M. Kitahara and Y. Katoh, *J. Geophys. Res.: Space Phys.* **124**, 5568, <https://doi.org/10.1029/2019JA026493> (2019).
- <sup>28</sup>B. V. Chirikov, *Phys. Rep.* **52**, 263 (1979).
- <sup>29</sup>S. N. Walker, M. A. Balikhin, P. Canu, N. Cornilleau-Wehrin, and I. Moiseenko, *J. Geophys. Res.: Space Phys.* **120**, 8774, <https://doi.org/10.1002/2015JA021718> (2015).
- <sup>30</sup>B. Ni, J. Bortnik, R. M. Thorne, Q. Ma, and L. Chen, *J. Geophys. Res.: Space Phys.* **118**, 7740, <https://doi.org/10.1002/2013JA019260> (2013).
- <sup>31</sup>H. Zhao, B. Ni, X. Li, D. N. Baker, W. R. Johnston, W. Zhang, Z. Xiang, X. Gu, A. N. Jaynes, S. G. Kanekal, J. B. Blake, S. G. Claudepierre, M. A. Temerin, H. O. Funsten, G. D. Reeves, and A. J. Boyd, *Nat. Phys.* **15**, 367 (2019).
- <sup>32</sup>Q. Ma, W. Li, R. M. Thorne, J. Bortnik, G. D. Reeves, C. A. Kletzing, W. S. Kurth, G. B. Hospodarsky, H. E. Spence, D. N. Baker, J. F. Fennell, S. G. Claudepierre, and V. Angelopoulos, *J. Geophys. Res.: Space Phys.* **121**, 11737, <https://doi.org/10.1002/2016JA023311> (2016).
- <sup>33</sup>J. Li, Q. Ma, J. Bortnik, W. Li, X. An, G. D. Reeves, H. O. Funsten, H. Spence, D. N. Baker, and W. S. Kurth, *Geophys. Res. Lett.* **46**, 12675, <https://doi.org/10.1029/2019GL085562> (2019).
- <sup>34</sup>Y. K. Hsieh and Y. Omura, *J. Geophys. Res.: Space Phys.* **122**, 675, <https://doi.org/10.1002/2016JA023255> (2017).
- <sup>35</sup>Y. K. Hsieh, Y. Omura, and Y. Kubota, *J. Geophys. Res.: Space Phys.* **127**, e2021JA029583, <https://doi.org/10.1029/2021JA029583> (2022).